

# A fully discrete, kinetic energy consistent finite-volume scheme for compressible flows

Pramod K. Subbareddy\*, Graham V. Candler

Department of Aerospace Engineering and Mechanics, University of Minnesota, 107, Akerman Hall, 110, Union Street, Minneapolis, MN 55455, United States

## ARTICLE INFO

### Article history:

Received 6 June 2008

Received in revised form 22 September 2008

Accepted 16 October 2008

Available online 5 November 2008

### Keywords:

Compressible flow

Direct numerical simulation

Large-eddy simulation

Non-dissipative

Kinetic energy

Implicit time integration

Fully discrete

## ABSTRACT

A robust, implicit, low-dissipation method suitable for LES/DNS of compressible turbulent flows is discussed. The scheme is designed such that the discrete flux of kinetic energy and its rate of change are consistent with those predicted by the momentum and continuity equations. The resulting spatial fluxes are similar to those derived using the so-called skew-symmetric formulation of the convective terms. Enforcing consistency for the time derivative results in a novel density weighted Crank–Nicolson type scheme. The method is stable without the addition of any explicit dissipation terms at very high Reynolds numbers for flows without shocks. Shock capturing is achieved by switching on a dissipative flux term which tends to zero in smooth regions of the flow. Numerical examples include a one-dimensional shock tube problem, the Taylor–Green problem, simulations of isotropic turbulence, hypersonic flow over a double-cone geometry, and compressible turbulent channel flow.

© 2008 Elsevier Inc. All rights reserved.

## 1. Introduction

Ideally, numerical schemes used in large-eddy simulations (LES) of compressible flow have the following properties: they are (i) conservative, (ii) capable of capturing shocks, (iii) non-dissipative in regions of the flow that are smooth, and (iv) stable. Conditions (i) and (ii) are not too problematic: discretizing the conservative form of the governing equations ensures that mass, momentum and total energy are conserved; shock capturing methods of various degrees of sophistication exist in the literature and are relatively well studied.

As for condition (iii), ‘low-dissipation’ schemes have been constructed [1,2] by selectively switching on the dissipative portion of the numerical flux in regions of the flow where discontinuities are detected (the fluxes used in most shock capturing methods can be written as the sum of a symmetric, non-dissipative part and a dissipative portion). Detecting shocks and discontinuities in a robust and efficient manner is a topic of current research; however, several shock detecting ‘switches’ have been proposed (e.g. [1–5]) and have been shown to be effective over a range of flow conditions.

Assuming that the shock capturing and detection mechanisms function adequately, we are left with the problem of trying to ensure that the non-dissipative symmetric fluxes produce stable solutions. Numerical instability is especially problematic in non-dissipative LES of turbulent flows. By construction, these solutions typically have substantial energy at all the resolved wavenumbers – the Nyquist wavelength of the grid is usually close to the LES filter length scale, which is usually in the inertial range of the energy spectrum and has large energy content (both in theory and in the numerical solution, for

\* Corresponding author.

E-mail addresses: [pramod@aem.umn.edu](mailto:pramod@aem.umn.edu) (P.K. Subbareddy), [candler@aem.umn.edu](mailto:candler@aem.umn.edu) (G.V. Candler).

non-dissipative schemes). In these situations, aliasing errors due to the non-linear convective terms in the Navier–Stokes equations are significant and result in a ‘pile-up’ of energy in the aliased wavenumbers, eventually causing the solutions to blow up if they are not contained. Aliasing errors are usually associated with high-order methods (because low-order methods do not represent the largest wavenumbers accurately). Indeed, the first de-aliasing methods were designed for pseudo-spectral simulations [6,7]. However, low-order central difference approximations or symmetric finite-volume fluxes are also susceptible to instability and aliasing, and strategies to stabilize the solutions seem to work just as well for both high and low-order schemes.

For compressible flows, there are two main approaches to dealing with the stability problem. Firstly, writing the convective terms in the ‘skew-symmetric’ form results in reduced amplitude of the aliasing errors relative to the divergence and advective forms. This was shown using pseudo-spectral simulations of Burgers’ equation and compressible isotropic turbulence by Blaisdell et al. [8]. Ducros et al. [9] derived a set of second and fourth-order accurate, conservative ‘skew-symmetric-like’ fluxes for finite-volume methods, with de-aliasing in mind. The skew-symmetric splitting has also been used by [10–13], among others, for DNS and LES computations of compressible flows. In a recent paper, Kennedy and Gruber [14] discussed skew-symmetric formulations for the cubic non-linearities that are found in the convective terms of the compressible Navier–Stokes equations. A discussion on the use of skew-symmetric forms for incompressible flows, and relevant references, can be found in the review paper by Moin and Mahesh [15].

The second approach uses the idea of secondary conservation laws [16,17] – essentially additional equations in conservation law form for quantities (such as entropy) that can be derived from the primary conservation equations. Under certain conditions, such secondary quantities are called entropy functions and the corresponding fluxes are entropy fluxes (among others, entropy functions have been studied in [16,18–20]). An entropy function can be used to generate a vector of ‘entropy variables’ which can be mapped uniquely with the vector of conserved variables. For example, the entropy function  $\mathcal{U} = \rho s$  can be used to generate the vector of entropy variables  $W = \partial \mathcal{U} / \partial U$ , where  $U$  is the vector of conserved variables. The notion of entropy variables is used to enhance numerical stability in two distinct ways. Firstly, theorems due to Godunov [16] and Mock [20] show that entropy functions and symmetrization are closely linked – a change of variables from  $U$  to  $W$  symmetrizes the equations of motion. The symmetric form is useful because it permits one to derive a continuous energy estimate [21] which bounds a norm of the solution in time. This formulation was used by Gerritsen and Olsson [22] and by Yee et al. [1] (the SHOEC scheme) and produced stable solutions for a broad range of compressible flows. In a different approach, the entropy function theory is used to constrain the fluxes of the Euler equations in such a way that the secondary conservation law is also discretely satisfied. If  $\rho s$  is used as the entropy function, this is essentially a means of ensuring that the second law of thermodynamics is satisfied by the discretized Euler equations. Given a set of entropy variables, a condition that the Euler flux has to satisfy to ensure discrete secondary conservation of the corresponding entropy function can be derived. Explicit solutions for the ‘entropy-satisfying’ Euler fluxes were derived by Tadmor [23] and by Roe [24]. These schemes have been used to examine shock tube problems (with the carbuncle phenomenon in mind), and we are not aware of the use of these fluxes in turbulent flow calculations, so the effect on stability for LES calculations is uncertain.

Honein and Moin [25] used a combination of both ideas. The convective terms of the momentum equation were written in skew-symmetric form; in addition, an equation for the internal energy was derived from the conservation equation for entropy ( $\rho s$ ), with the convective terms in the entropy equation also written in the skew-symmetric form. This aims to ensure that, in addition to kinetic energy, the average of  $\rho s^2$  over the domain is not spuriously affected by the non-linear convective terms. They compared their scheme with various other methods (including the SHOEC scheme and the skew-symmetric-like formulation of [9]) using coarse grid simulations of isotropic turbulence and demonstrated its superior stability at high Reynolds numbers.

In this paper, we primarily consider the equation for kinetic energy ( $\rho k = \rho u_i u_i / 2$ ). For incompressible flows, the evolution of kinetic energy is implicitly represented by the evolution of the velocity: an equation for kinetic energy can be derived by multiplying the momentum equations by the velocity components and summing. In the paper by Mahesh et al. [26], it is shown that writing the discrete fluxes of the momentum equations in a form which makes the implied flux of kinetic energy conservative ensures that the net change of kinetic energy in the computational domain is due only to boundary contributions and viscous dissipation. This vastly improves the stability of the calculations.

For compressible flows, the equation for kinetic energy transport is derived from the conservation equations for density and momentum: it is not an independent equation. However, in most formulations, it is combined with the internal energy to give us a set of equations in conservation form, which is important for flows with shocks. We concentrate on the terms representing the flux of kinetic energy,  $\partial \rho k u_j / \partial x_j$ , and its rate of change,  $\partial \rho k / \partial t$ , which appear in the total energy equation. It is easy to show that these terms can be obtained from the corresponding terms in the continuity and momentum equations, for the PDEs: this is what is meant by ‘consistency’ in the title. For the spatial fluxes, ensuring that the discrete equations are consistent as well gives us a simple set of constraints on the fluxes, similar to the incompressible flow formulation in [26], as well as the skew-symmetric form presented in [9]. Ensuring that the discrete time derivatives are consistent results in a novel density weighted Crank–Nicolson like scheme.

The paper is organized as follows. This introductory section is concluded by describing the governing equations and the terminology used. Section 2 is concerned with the kinetic energy consistent formulation. Section 3 outlines the shock capturing method and Section 4 discusses the implicit time integration method used. Numerical examples are presented in Section 5 and the paper concludes with a summary in Section 6.

### 1.1. Governing equations and nomenclature

The Navier–Stokes equations for a perfect gas, written in divergence form are

$$\frac{\partial U}{\partial t} + \frac{\partial \tilde{F}_j}{\partial x_j} = 0, \quad (1)$$

where the conserved variables,  $U$ , and the corresponding fluxes,  $\tilde{F}_j$ , are given by

$$U = \begin{pmatrix} \rho \\ \rho u \\ \rho v \\ \rho w \\ E \end{pmatrix} \quad \text{and} \quad \tilde{F}_j = \begin{pmatrix} \rho u_j \\ \rho u u_j + p \delta_{1j} - \sigma_{1j} \\ \rho v u_j + p \delta_{2j} - \sigma_{2j} \\ \rho w u_j + p \delta_{3j} - \sigma_{3j} \\ (E + p) u_j - \sigma_{kj} u_k + q_j \end{pmatrix}.$$

The variables have the usual meanings:  $\rho$ ,  $u_j$ ,  $p$  and  $T$  are the density, velocity, pressure and temperature. For the velocity field, the notation  $(u, v, w)$  is used interchangeably with  $u_{j \in \{1,2,3\}}$ . The pressure is assumed to follow the ideal gas law,  $p = \rho RT$ . The total energy is the sum of the internal and kinetic energies,  $E = \rho e + \rho k$ , where  $k = u_i u_i / 2$  and  $e = C_v T$ .  $R$  and  $C_v$  are the gas constant and specific heat at constant volume, respectively. The ratio of the specific heat at constant pressure,  $C_p$  to  $C_v$  is  $\gamma = C_p / C_v$  and is assumed to be 1.4. The viscous stress tensor,  $\sigma_{ij}$ , and the heat conduction vector,  $q_j$  are

$$\sigma_{ij} = \mu \left( \frac{\partial u_i}{\partial x_j} + \frac{\partial u_j}{\partial x_i} \right) - \frac{2}{3} \mu \frac{\partial u_k}{\partial x_k} \delta_{ij} \quad \text{and} \quad q_j = \kappa \frac{\partial T}{\partial x_j}.$$

The viscosity is given by Sutherland's law,  $\mu = \mu_0 T^{3/2} / (T + T_0)$ , by a power law,  $\mu = \mu_0 (T / T_0)^\alpha$ , where  $\mu_0$ ,  $T_0$  and  $\alpha$  are constants, or is set to a constant for certain low Mach number flows. The thermal conductivity,  $\kappa$ , is assumed to be related to  $\mu$  through a constant Prandtl number,  $\text{Pr} = \mu C_p / \kappa$ , assumed to be 0.72. Integrating (1) over the control volumes defined by the grid and using Gauss' theorem gives the standard semi-discrete finite-volume formulation

$$\frac{\partial U_i}{\partial t} + \frac{1}{V_i} \sum_{\text{faces}} \tilde{F}'_f S_f = 0. \quad (2)$$

Fig. 1 shows the nomenclature used: the subscript  $i$  refers to the cell-center and  $\text{nbr}$  is a (generic) neighbor of cell  $i$  at the face  $f$ .  $S_f$  is the area of face  $f$  and the unit normal to a face,  $\hat{s}$  (oriented away from the cell interior), has direction cosines  $(s_x, s_y, s_z)$ .  $V_i$  is the volume of cell  $i$ . Primes are used to denote the projection of a vector onto the unit normal at a face: e.g.,  $u'_f = u_j s_j = u s_x + v s_y + w s_z$  and  $\tilde{F}' = \tilde{F}_j s_j$ . The flux  $\tilde{F}'$  is split into inviscid (convective terms and pressure) and viscous (diffusive terms and heat conduction) parts,  $\tilde{F}' = F' + F'_v$ , where  $F'_v$  is the viscous component.

### 2. A kinetic energy consistent flux

The kinetic energy,  $\rho k = \rho(u^2 + v^2 + w^2)/2$ , is not an 'entropy function' (in the sense of [16,18–20]): the vector  $\partial(\rho k)/\partial U = (-k, u, v, w, 0)^\top$  clearly does not have a one-to-mapping with the vector of conserved variables,  $U$ . Moreover, kinetic energy is balanced with the internal energy through the equation for conservation of total energy. Nevertheless, we can try and ensure that the convective fluxes in the Euler equations do not artificially produce kinetic energy – the same reasons that are used to justify writing the convective terms in skew-symmetric form.

A transport equation for kinetic energy can be derived using the continuity and momentum equations. Using the notation  $\mathbb{U} = (\rho, \rho u, \rho v, \rho w)^\top$  and  $\mathbb{F}_j = (\rho u_j, \rho u u_j, \rho v u_j, \rho w u_j)^\top$  to denote the restriction of the full set of conserved variables,  $U$ , and

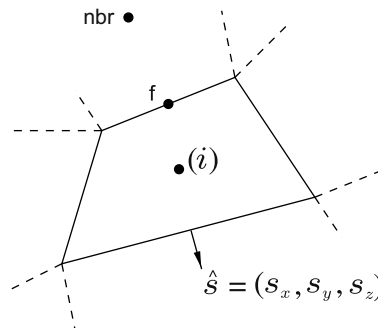


Fig. 1. Nomenclature.  $i$  denotes the cell-center,  $\text{nbr}$  is a neighbor of  $i$  at face  $f$ .

the fluxes  $F$  to just the density and momentum portions (neglecting the pressure), the kinetic energy equation can be derived from the Euler equations using

$$\left(\frac{\partial \rho k}{\partial \mathbb{U}}\right)^T \cdot \frac{D\mathbb{U}}{Dt} = \frac{D\rho k}{Dt},$$

where  $D(\cdot)/Dt$  denotes  $\partial(\cdot)/\partial t + \partial(\cdot)u_j/\partial x_j$ . Expanding the above and discretizing, we get, for cell  $i$ ,

$$[-k_i \quad u_i \quad v_i \quad w_i] \left\{ \frac{\partial}{\partial t} \underbrace{\begin{bmatrix} \rho \\ \rho u \\ \rho v \\ \rho w \end{bmatrix}}_{\mathbb{U}_i} + \frac{1}{V_i} \sum_f \underbrace{\begin{bmatrix} \rho u' \\ \rho u u' \\ \rho v u' \\ \rho w u' \end{bmatrix}}_{\mathbb{F}'_f} S_f \right\} = \frac{\partial(\rho k)_i}{\partial t} + \frac{1}{V_i} \sum_f (\rho k u' S)_f \quad (3)$$

Initially, we adopt a semi-discrete approach and examine the spatial terms separately from the time derivatives. Equating the convective fluxes in the equation above requires

$$[-k_i \quad u_i \quad v_i \quad w_i] \sum_f \begin{bmatrix} \rho u' \\ \rho u u' \\ \rho v u' \\ \rho w u' \end{bmatrix}_f S_f = \sum_f (\rho k u' S)_f.$$

On the left hand side, pull the vector  $\partial(\rho k)/\partial \mathbb{U}$  inside the summation and rearrange to get

$$\sum_f \left\{ [-\bar{k} \quad \bar{u} \quad \bar{v} \quad \bar{w}]_f \mathbb{F}'_f S_f - \underbrace{\frac{1}{2} [-\Delta k \quad \Delta u \quad \Delta v \quad \Delta w]_f \mathbb{F}'_f S_f}_A \right\} = \sum_f (\rho k u' S)_f, \quad (4)$$

where  $\mathbb{F}'$  is the numerical flux to be determined, the over-bar denotes the symmetric spatial average at a face, ( $\bar{a}_f = (a_i + a_{nbr})/2$ ) and  $\Delta$  represents the spatial difference ( $\Delta a = a_{nbr} - a_i$ ). Assume that the flux  $\mathbb{F}'_f$  is consistent and conservative. (In the sense that  $F(\cdots, U, U, \cdots) = F(U)$  and  $F(U_i, U_{nbr}) = F(U_{nbr}, U_i)$ .) Then the first term in the summation above is an acceptable representation of the convective flux of the kinetic energy (the right hand side of the above equation). This implies that we need to find a flux  $\mathbb{F}'_f$  such that the term marked  $A$  in the equation is identically zero. That is,

$$\sum_f [-\Delta k \quad \Delta u \quad \Delta v \quad \Delta w]_f \mathbb{F}'_f S_f = 0.$$

This is always true if we adopt the form

$$\mathbb{F}'_f = \rho_f u'_f \begin{bmatrix} 1 \\ \bar{u} \\ \bar{v} \\ \bar{w} \end{bmatrix}, \quad (5)$$

due to the identity  $\Delta k = \bar{u}\Delta u + \bar{v}\Delta v + \bar{w}\Delta w$ . The values of  $\rho_f$  and  $u'_f$  are left undetermined, except for the requirement that they be symmetric. The flux of kinetic energy is inferred from Eq. (4) to be

$$\sum_f (\rho k u' S)_f = \sum_f (-\bar{k} + \bar{u}^2 + \bar{v}^2 + \bar{w}^2)_f (\rho u' S)_f \equiv \sum_f \frac{1}{2} (u_i u_{nbr} + v_i v_{nbr} + w_i w_{nbr}) (\rho u' S)_f. \quad (6)$$

Note that the convective flux terms prescribed above for the momentum equations are no different than the kinetic energy conserving fluxes used in incompressible flow codes (see for example [26]), except for the presence of density and the use of Eq. (6) for the kinetic energy flux in the total energy equation. Also, for second-order formulations, the form of the density and momentum fluxes (Eq. (5)) is similar to the skew-symmetric flux presented in [2].

### 2.1. Fully discrete formulation

Numerical tests show that time discretization is important if we are to gain an advantage from using the fluxes constructed above. The identity

$$[-k_i \quad u_i \quad v_i \quad w_i] \frac{\partial \mathbb{U}_i}{\partial t} = \frac{\partial(\rho k)_i}{\partial t},$$

which is true for the PDEs should, ideally, be true for the discrete equations as well. For incompressible flow, the use of a Crank–Nicolson like scheme is natural: if the term  $u_j \frac{\partial u_j}{\partial t}$  is discretized as

$$\frac{(u_j^{n+1} + u_j^n)_i}{2} \cdot \frac{(u_j^{n+1} - u_j^n)_i}{\Delta t},$$

it is exactly equal to  $(k^{n+1} - k^n)_i / \Delta t$ . That is, if the velocities,  $u_j$ , appearing in the momentum equation are written as the average of their values at time levels  $n$  and  $n + 1$ , the rate of change of kinetic energy is algebraically consistent with that predicted by the momentum equations (the kinetic energy equation is not actually solved in incompressible flow). As a consequence of the symmetry of the flux terms, the net change in kinetic energy only appears through the boundary fluxes. This bounding property dramatically improves the stability of the scheme.

For the compressible Euler equations (and for variable density incompressible flow equations), we have to try to ensure that the relation

$$u_j \frac{\partial \rho u_j}{\partial t} - k \frac{\partial \rho}{\partial t} = \frac{\partial \rho k}{\partial t} \quad (7)$$

is true discretely. A straightforward use of average values in time, as before, does not yield a discrete equality, as can be readily verified:

$$\frac{(u_j^{n+1} + u_j^n)_i}{2} \cdot \frac{(\rho u_j)_i^{n+1} - (\rho u_j)_i^n}{\Delta t} - \frac{k_i^{n+1} + k_i^n}{2} \cdot \frac{\rho_i^{n+1} - \rho_i^n}{\Delta t} \neq \frac{(\rho k)_i^{n+1} - (\rho k)_i^n}{\Delta t}.$$

However, as we show below, if we use density weighted (in time) velocities in the equation above, we can exactly satisfy the above relation. We discretize Eq. (7), above, and ask the question: is there a unique vector  $[-k^*, u^*, v^*, w^*]$  such that

$$[-k^* \quad u^* \quad v^* \quad w^*]_i \frac{1}{\Delta t} \begin{bmatrix} \rho^{n+1} - \rho^n \\ (\rho u)^{n+1} - (\rho u)^n \\ (\rho v)^{n+1} - (\rho v)^n \\ (\rho w)^{n+1} - (\rho w)^n \end{bmatrix}_i = \frac{(\rho k)_i^{n+1} - (\rho k)_i^n}{\Delta t}. \quad (8)$$

Roe's parameter vector [27] was originally used by him to connect the jump in flux across an interface to the corresponding jump in the vector of conserved quantities through a matrix constructed from a suitable average of variables on either side of the interface ( $\Delta F_i = A_{ij} \Delta U_j$ ). The key element of Roe's construction is an elegant transformation which permits one to express the vector of conserved quantities and  $\rho k$  as quadratic products of the elements of a parameter vector

$$\mathbb{Z} = \sqrt{\rho} [1 \quad u \quad v \quad w].$$

The algebraic identity  $\Delta(pq) = \bar{p} \Delta q + \bar{q} \Delta p$  is obviously true for arbitrary jumps in  $p$  and  $q$ . (This is not as trivial as it appears. For example, there is no corresponding unique expression for triple products.)

Denoting the elements of  $\mathbb{Z}$  by  $z_{j \in \{1,2,3,4\}}$ , we express

$$[\rho \quad \rho u \quad \rho v \quad \rho w \quad \rho k] = \begin{bmatrix} z_1^2 & z_1 z_2 & z_1 z_3 & z_1 z_4 & \frac{z_1^2 + z_2^2 + z_3^2}{2} \end{bmatrix}.$$

This allows us to rewrite Eq. (8) as

$$[-k^* \quad u^* \quad v^* \quad w^*] \frac{1}{\Delta t} \begin{bmatrix} 2\bar{z}_1 \Delta z_1 \\ \bar{z}_1 \Delta z_2 + \bar{z}_2 \Delta z_1 \\ \bar{z}_1 \Delta z_3 + \bar{z}_3 \Delta z_1 \\ \bar{z}_1 \Delta z_4 + \bar{z}_4 \Delta z_1 \end{bmatrix}_i = \frac{(\bar{z}_2 \Delta z_2 + \bar{z}_3 \Delta z_3 + \bar{z}_4 \Delta z_4)}{\Delta t},$$

which can be arranged to read

$$[-k^* \quad u^* \quad v^* \quad w^*] \frac{1}{\Delta t} \begin{bmatrix} 2\bar{z}_1 & 0 & 0 & 0 \\ \bar{z}_2 & \bar{z}_1 & 0 & 0 \\ \bar{z}_3 & 0 & \bar{z}_1 & 0 \\ \bar{z}_4 & 0 & 0 & \bar{z}_1 \end{bmatrix} \begin{bmatrix} \Delta z_1 \\ \Delta z_2 \\ \Delta z_3 \\ \Delta z_4 \end{bmatrix} = \frac{1}{\Delta t} [0 \quad \bar{z}_2 \quad \bar{z}_3 \quad \bar{z}_4] \begin{bmatrix} \Delta z_1 \\ \Delta z_2 \\ \Delta z_3 \\ \Delta z_4 \end{bmatrix}. \quad (9)$$

Since the above should be true for arbitrary jumps  $\Delta z_j$ , we can solve

$$[-k^* \quad u^* \quad v^* \quad w^*] = [0 \quad \bar{z}_2 \quad \bar{z}_3 \quad \bar{z}_4] \begin{bmatrix} 2\bar{z}_1 & 0 & 0 & 0 \\ \bar{z}_2 & \bar{z}_1 & 0 & 0 \\ \bar{z}_3 & 0 & \bar{z}_1 & 0 \\ \bar{z}_4 & 0 & 0 & \bar{z}_1 \end{bmatrix}^{-1} = \begin{bmatrix} -\frac{\bar{z}_2^2 + \bar{z}_3^2 + \bar{z}_4^2}{2\bar{z}_1^2} & \frac{\bar{z}_2}{\bar{z}_1} & \frac{\bar{z}_3}{\bar{z}_1} & \frac{\bar{z}_4}{\bar{z}_1} \end{bmatrix}.$$

Expanding the terms, we get

$$\begin{bmatrix} -k^* \\ u^* \\ v^* \\ w^* \end{bmatrix} = \begin{bmatrix} -\frac{u^{*2} + v^{*2} + w^{*2}}{2} \\ \frac{\sqrt{\rho^{n+1}}u^{n+1} + \sqrt{\rho^n}u^n}{\sqrt{\rho^{n+1}} + \sqrt{\rho^n}} \\ \frac{\sqrt{\rho^{n+1}}v^{n+1} + \sqrt{\rho^n}v^n}{\sqrt{\rho^{n+1}} + \sqrt{\rho^n}} \\ \frac{\sqrt{\rho^{n+1}}w^{n+1} + \sqrt{\rho^n}w^n}{\sqrt{\rho^{n+1}} + \sqrt{\rho^n}} \end{bmatrix}. \quad (10)$$

These values are used in the expression for the convective fluxes (Eq. (5)) and the kinetic energy portion of the flux of total energy, giving the convective flux

$$\begin{bmatrix} \rho u' \\ \rho u'u \\ \rho u'v \\ \rho u'w \\ \rho u'k \end{bmatrix}_f = \rho_f u'_f \begin{bmatrix} 1 \\ \frac{u^*}{\rho_f} \\ \frac{v^*}{\rho_f} \\ \frac{w^*}{\rho_f} \\ \frac{k^*}{\rho_f} \end{bmatrix}_f,$$

where  $\overline{(\cdot)}$  is a spatial average, as before, and  $\widetilde{k^*} = -k^* + \overline{u^{*2}} + \overline{v^{*2}} + \overline{w^{*2}}$  (see Eq. (6)). The terms  $\rho_f$  and  $u'_f$ , which were left undetermined, are evaluated as  $\rho_f = (\overline{\rho^n} + \overline{\rho^{n+1}})/2$  and  $u'_f = (\overline{u^*s_x} + \overline{v^*s_y} + \overline{w^*s_z})_f$ .

The pressure and internal energy terms in the momentum and energy fluxes remain to be specified. In keeping with the time and space centered evaluation of the convective fluxes above, it seems natural to write the pressure in the momentum flux as  $p_f = (\overline{p^n} + \overline{p^{n+1}})/2$ . However, this leads to oscillatory solutions. The problem is especially noticeable in problems with solutions that have energetic high frequency modes. Biasing the pressure flux toward the time level  $n+1$  (which is equivalent to adding a small amount of dissipation) by using the form

$$p_f = \frac{(1-\epsilon)\overline{p^n} + (1+\epsilon)\overline{p^{n+1}}}{2},$$

where  $\epsilon$  is a small number, leads to cleaner solutions. Choosing  $\epsilon$  to be proportional to  $\Delta t$  would make the dissipation due to the pressure biasing  $\mathcal{O}(\Delta t)^2$ : a similar approach is used in the paper by Wall et al. [28]. Note that for the flow cases considered here, fully upwinding the pressure term in time ( $\epsilon = 1$ ) did not have an appreciable effect on the dissipation levels. One of the reviewers for this paper makes the point that ensuring a “consistent” exchange of internal and kinetic energy through the pressure terms in the energy and momentum equations might help resolve this problem. Writing Gibbs’s equation ( $Tds = de - p/\rho^2 d\rho$ ) in a “conservation” form gives the relation

$$T \frac{D\rho s}{Dt} + \left( e - sT + \frac{p}{\rho} \right) \frac{D\rho}{Dt} = \frac{D\rho e}{Dt} + p \frac{\partial u_i}{\partial x_j},$$

where  $D(\cdot)/Dt \equiv \partial(\cdot)/\partial t + \partial(\cdot)u_j/\partial x_j$ . The right hand side consists of the time derivative, the convective flux and the pressure–velocity coupling terms in the equation for internal energy. For inviscid flow, this should be zero and this is true only if both the entropy ( $\rho s$ ) and the density are discretely conserved (i.e.  $D\rho s/Dt = 0$  and  $D\rho/Dt = 0$ ). This suggests that erroneous entropy production affects the correct exchange of kinetic and internal energies. Note that the dissipation introduced by the pressure biasing helps prevent the net entropy in the computational volume from decreasing. Perhaps ensuring that entropy is not spuriously produced by the fluxes (and the time discretization) would help resolve the question of why we need to bias the pressure terms in time. We have not hit upon a satisfactory finite-volume scheme that is both kinetic energy consistent and entropy conservative (in a fully discrete sense).

The flux of internal energy which appears in the energy equation is evaluated as  $\rho_f u'_f e_f$ , where  $e_f = C_v(\overline{T^n} + \overline{T^{n+1}})/2$ . The viscous fluxes at a face,  $F'_{v,f}$  involve the first derivatives of the primitive variables ( $\rho, u, v, w, T$ ) at the face. For calculations on structured grids, these derivatives are evaluated with respect to the general curvilinear system ( $\xi, \eta, \zeta$ ) and then transformed to the Cartesian coordinate system ( $x, y, z$ ). Details can be found in Hirsch [29].

### 3. Shock capturing

Shock capturing is accomplished by adding a dissipative flux

$$F'_{f,diss} = \alpha_{diss} D_f, \quad (11)$$

where  $D_f$  is the dissipative portion of a standard shock capturing scheme and  $0 \leq \alpha_{diss} \leq 1$  is a switch which takes on values close to zero in smooth regions of the flow and values close to one at discontinuities. A robust expression for this shock detection switch, suggested by Ducros et al. [2], is given by

$$\alpha_{diss} = \min \left( \frac{\theta^2}{\theta^2 + \omega^2 + \epsilon}, 1 \right), \quad (12)$$

where  $\omega$  is the vorticity magnitude,  $\theta$  is the divergence of the velocity and  $\epsilon$  is a small number that prevents division by zero. In regions of the flow where compressibility effects (represented by the dilatation) dominate, the switch assumes values close to one and the full magnitude of the dissipative flux is applied; the reverse happens in turbulent regions of the flow where the enstrophy is much larger than the dilatation. Among other switches in use, many involve combinations of pressure and density gradients (e.g. [3,11]). A switch based on the jump in Mach number across the face is suggested by [30]. For multi-dimensional calculations, for which the terms involved are well defined, we use the Ducros switch; for one-dimensional problems with shocks, we use a simpler shock detector based on pressure and density gradients.

The dissipative portion of the modified Steger–Warming scheme [31] is used for the term  $D_f$ . The first-order modified Steger–Warming flux is given by  $F'_f = (RA^+R^{-1})_f \cdot U_i + (RA^-R^{-1})_f \cdot U_{nbr}$ , where  $R$  is the right eigenvector matrix of the flux Jacobian  $A = \partial F / \partial U$ ,  $A$  is the diagonal matrix of eigenvalues of  $A$ , and  $A^\pm$  denote the splitting of the eigenvalues into positive and negative parts,  $(A \pm |A|)/2$  (the subscript  $f$  indicates that the matrices are computed using average values at the face). We can expand the flux above to get

$$F'_f = (RAR^{-1})_f \cdot \left( \frac{U_i + U_{nbr}}{2} \right) - \frac{1}{2} (R|A|R^{-1})_f \cdot (U_{nbr} - U_i).$$

The first term on the right hand side is the symmetric part of the modified Steger–Warming flux. This is replaced with the kinetic energy consistent flux described in the previous sections. The dissipative part,

$$D_f = -\frac{1}{2} (R|A|R^{-1})_f \cdot (U_{nbr} - U_i), \quad (13)$$

is multiplied by the switch  $\alpha_{\text{diss},f}$  to give  $F'_{f,\text{diss}}$ , where  $\alpha_{\text{diss},f} = \max(\alpha_{\text{diss},i}, \alpha_{\text{diss},nbr})$ . Note that if the matrices  $R$  and  $A$  are evaluated using Roe-averages [27], the modified Steger–Warming flux and the commonly used Roe-flux are identical. In practice, the terms  $U_{nbr}$  and  $U_i$  are replaced with higher order interpolates,  $U_R$  and  $U_L$ , which are constructed using, for e.g., a second-order TVD-MUSCL [32] scheme. Also, to avoid problems caused when the eigenvalues are close to zero (at sonic and stagnation points), the modified eigenvalues

$$\lambda_k^\pm = \frac{\lambda_k \pm \sqrt{\lambda_k^2 + \delta c^2}}{2},$$

are used instead. Here,  $\delta$  is a small number (this is flow dependent and is usually in the range 0.1–0.2) and  $c$  is the local speed of sound.

#### 4. Time integration

The discrete system of equations we are solving is

$$\frac{U_i^{n+1} - U_i^n}{\Delta t} + \frac{1}{V_i} \sum_f F'_f(U_f^n, U_f^{n+1}) S_f = 0, \quad (14)$$

where we are interested in finding  $U^{n+1}$  and  $U^n$  is assumed to be known.  $U_f$  indicates an average over the cells neighboring face  $f$ ; for example  $U_f = (U_i^* + U_{nbr}^*)/2$ , where the star superscripts denote averages in time, as in Eq. (10).

##### 4.1. Explicit iteration

A simple way to solve the system is by the explicit iteration

$$U_i^{n+1,k+1} = U_i^n - \frac{\Delta t}{V_i} \sum_f F'_f(U_f^n, U_f^{n+1,k}) S_f,$$

where  $k$  is an iteration index and the initial value  $U^{n+1,0}$  is assumed to be  $U^n$ . The iteration is stopped when an integral measure of the residual drops below some threshold:

$$\text{norm}(U^{n+1,k+1} - U^{n+1,k}) < \epsilon.$$

A scalar version of the set of equations would be  $(u^{n+1} - u^n)/\Delta t = f((u^{n+1} + u^n)/2)$ . Pierce [33] describes the stability limits of the linear model problem,  $du/dt = \lambda u$ , solved using the above Crank–Nicolson like formulation and shows that a minimum of two iterations is required for second-order accuracy. In practice, the number of iterations to reach a prescribed tolerance is larger, especially for flows with shocks.



#### 4.2. Implicit method

The time step allowed by explicit schemes is limited by the maximum wave speed  $|u| + c$  and the grid size  $\Delta x$

$$\Delta t_{\text{exp}} < \Delta x / (|u| + c).$$

For turbulent flows, where the relevant velocity scale is the local velocity ( $u$ ) rather than the maximum wave speed ( $|u| + c$ ), the time step we would ideally like to use is proportional to  $\Delta x / u$ . Dividing this by the allowable explicit time step,  $\Delta t_{\text{exp}}$ , results in a CFL number that scales as  $1 + 1/M$ , where  $M$  is the Mach number (if we are not interested in capturing the acoustics). Thus, the number of time steps required by an explicit scheme would be larger by a factor of  $\mathcal{O}(1/M)$ , which can be unmanageably large for flows with low Mach number regions. In most aerodynamic applications, the presence of shear layers requires grids that have high aspect ratio cells: the large variation in  $\Delta x$  imposes a severe time step restriction as well. For both the reasons above, implicit time integration schemes are essential for efficient calculations of turbulent compressible flows.

We use an iterative scheme, whereby the solution is driven to a pseudo-steady state within each time step using a number of sub-iterations. The implicit equations are

$$\frac{(1 + \varphi)U_i^{n+1,s+1} - (1 + 2\varphi)U_i^n + \varphi U_i^{n-1}}{\Delta t} + \frac{1}{V_i} \sum_f F'_f(U_f^n, U_f^{n+1,s+1}) S_f = 0. \quad (15)$$

Setting  $\varphi = 0$  gives the first-order backward Euler formula and  $\varphi = 1/2$  gives the second-order backward difference formula (BDF2) for the time derivative;  $s$  is the sub-iteration index. The solution is obtained in two stages.

- First, set  $\varphi = 1/2$  and solve the system

$$\frac{3U_i^{n+1,s=0} - 4U_i^n + U_i^{n-1}}{2\Delta t} + \frac{1}{V_i} \sum_f F'_f(U_f^{n+1,s=0}) S_f = 0 \quad (16)$$

for  $U^{n+1,s=0}$ .

- Next, use the initial guess and iterate till the system (14) is satisfied to a preset tolerance

DO

SOLVE:

$$\frac{U_i^{n+1,s+1} - U_i^n}{\Delta t} + \frac{1}{V_i} \sum_f F'_f(U_f^n, U_f^{n+1,s+1}) S_f = 0. \quad (17)$$

IF  $\text{norm}(U^{n+1,s+1} - U^{n+1,s}) \leq \text{tol}_s$  EXIT

END DO

At the end of the above steps, we set  $U^{n+1} = U^{n+1,s+1}$ . For steady state problems, or for rough, first attempts at a solution, the iterative stage of the process can be dispensed with.

The implicit equations (16) and (17) are solved using the full-matrix point relaxation (FMPR) algorithm [34], described in the next section. The flux linearizations

$$F'(U^{n+1}) \approx F'(U^n) + \frac{\partial F'(U^n)}{\partial U^n} \cdot \overbrace{(U^{n+1} - U^n)}^{\delta U^n} \quad (18a)$$

$$F'(U^n, U^{n+1,s+1}) \approx F'(U^n, U^{n+1,s}) + \frac{\partial F'(U^n, U^{n+1,s})}{\partial U^{n+1,s}} \cdot \underbrace{(U^{n+1,s+1} - U^{n+1,s})}_{\delta U^{n,s}}, \quad (18b)$$

are used to estimate fluxes which involve the solution at a future time level in Eqs. (16) and (17), respectively. For the Euler equations, the flux is the sum of the symmetric and dissipative portions:  $F'_f = F'_{f,\text{sym}} + F'_{f,\text{diss}}$ ; linearizing the flux as in Eq. (18a) and using the definition of the dissipative flux (Eqs. (11) and (13)) gives

$$F'_f(U_f^{n+1}) \approx F'_f(U_f^n) + \underbrace{\left[ \frac{\partial F'_{f,\text{sym}}(U_f^n)}{\partial U_i^n} + \left( \frac{\alpha_{\text{diss}}}{2} R |A| R^{-1} \right)_f^n \right]}_{A_{f,i,\alpha_{\text{diss}}}^+} \cdot \delta U_i^n + \underbrace{\left[ \frac{\partial F'_{f,\text{sym}}(U_f^n)}{\partial U_{\text{nbr}}^n} - \left( \frac{\alpha_{\text{diss}}}{2} R |A| R^{-1} \right)_f^n \right]}_{A_{f,i,\alpha_{\text{diss}}}^-} \cdot \delta U_{\text{nbr}}^n, \quad (19)$$

where  $\alpha_{\text{diss}}$  is the shock detecting switch. We label the matrix multiplying  $\delta U_i$  (the diagonal terms) as  $A_f^+$  and the off-diagonal matrix as  $A_f^-$ . (The corresponding expression for Eq. (18b) is similar.)

##### 4.2.1. Point relaxation algorithm

Substitute the linearization (19) in Eq. (16) to get

$$\underbrace{\left[ \frac{3\mathbf{I}}{2\Delta t} + \frac{1}{V_i} \sum_f \{ A_{f,i,\alpha_{\text{diss}}}^+(U_f^n) S_f \} \right]}_{\text{Diagonal terms}} \cdot \delta U_i^n + \underbrace{\frac{1}{V_i} \sum_f \{ A_{f,i,\alpha_{\text{diss}}}^-(U_f^n) \cdot \delta U_{\text{nbr}}^n S_f \}}_{\text{Off-diagonal terms}} = -\frac{1}{V_i} \sum_f F'_f(U_f^n) S_f + \frac{\delta U_i^{n-1}}{2\Delta t}, \quad (20)$$



where  $\mathbb{I}$  is the identity matrix. A number of methods could be used to solve this system of equations. We propose to use the full-matrix point relaxation (FMPR) algorithm [34], which consists of two steps (the subscript  $\alpha_{\text{diss}}$  on the Jacobians is omitted below, for clarity):

1. Find a guess solution  $\delta U^{n,k=0}$  by neglecting the off-diagonal terms. That is, find

$$\delta U_i^{n,k=0} = \left[ \frac{3\mathbb{I}}{2\Delta t} + \frac{1}{V_i} \sum_f \{A_f^+(U_f^n) S_f\} \right]^{-1} \left[ -\frac{1}{V_i} \sum_f F'_f(U_f^n) S_f + \frac{\delta U_i^{n-1}}{2\Delta t} \right].$$

2. Include the effect of the off-diagonal terms in a series of relaxation steps

**while**  $\text{res} \geq \text{tol}_k$  **do**

$$\delta U_i^{n,k+1} = \left[ \frac{3\mathbb{I}}{2\Delta t} + \frac{1}{V_i} \sum_f \{A_f^+(U_f^n) S_f\} \right]^{-1} \left[ -\frac{1}{V_i} \sum_f F'_f(U_f^n) S_f + \frac{\delta U_i^{n-1}}{2\Delta t} - \frac{1}{V_i} \sum_f \{A_f^-(U_f^n) \cdot \delta U_{\text{nbr}}^{n,k} S_f\} \right],$$

**end while**

where the residual is defined as  $\text{res} = \text{norm}(\delta U^{n,k} - \delta U^{n,k-1})$ , and the tolerance,  $\text{tol}_k$ , is problem dependent (typically, we continue the relaxation iterations until the residual has fallen by two or three orders of magnitude from its initial value). The Jacobian matrices are ‘frozen’ at time level  $n$ , for simplicity. Note that the relaxation iteration index  $k$  is not to be confused with the sub-iteration index  $s$ .

The following points concerning the stability and dissipative properties of the algorithm must be noted:

- When the dissipation switch  $\alpha_{\text{diss}}$  is small, using the Jacobians,  $A_{f,\alpha_{\text{diss}}}^\pm$ , makes the implicit algorithm unstable. This is because the diagonal dominance of the implicit operator is not guaranteed for small values of the switch,  $\alpha_{\text{diss}}$ . A recent paper by Kim and Kwon [35] discusses this problem in some detail. Setting the switch to 1 (for the flux Jacobians only) stabilizes the implicit routine, but at the cost of adding a dissipative term, as detailed below.
- Setting  $\alpha_{\text{diss}}$  to unity introduces a dissipative term since the LHS of the equation that is actually being solved is

$$\left[ \frac{3\mathbb{I}}{2\Delta t} + \frac{1}{V_i} \sum_f \{A_{f,\alpha=1}^+(U_f^n) S_f\} \right] \cdot \delta U_i^n + \frac{1}{V_i} \sum_f \{A_{f,\alpha=1}^-(U_f^n) \cdot \delta U_{\text{nbr}}^n S_f\}. \quad (21)$$

Subtracting Eq. (21) from the LHS of (20) and simplifying leaves us with the terms

$$\frac{1}{V_i} \sum_f \left[ \left( \frac{1 - \alpha_{\text{diss}}}{2} R |A| R^{-1} S \right)_f \cdot (\delta U_{\text{nbr}} - \delta U_i) \right]. \quad (22)$$

By analogy with Eq. (13), these terms are identifiable with dissipation due to the choice of  $\alpha_{\text{diss}} = 1$  in the flux Jacobians. Although the magnitude of the implicit dissipation is small, the effect is noticeable over a large number of time steps. This problem is especially severe when the solution has energetic high frequency modes (as in high Reynolds number LES simulations).

- With  $\alpha_{\text{diss}} = 1$ , the Jacobians,  $A_{f,\alpha=1}^\pm$ , are interchangeable with the matrices  $A_f^\pm = R A^\pm R^{-1}$ , where  $A^\pm = (A \pm |A|)/2$ . The difference between these and the matrices in Eq. (19) is negligible, so there is no need to compute terms such as  $\partial F'_f / \partial U_i$ : the eigenvector matrices computed for the shock capturing part can be re-used.

#### 4.2.2. Sub-iteration to pseudo-steady state

Now that we have an initial guess for Eq. (15), we can proceed with the sub-iterations to a pseudo-steady state. Use the linearization (18b) in Eq. (17) to get

$$\begin{aligned} & \left[ \frac{\mathbb{I}}{\Delta t} + \frac{1}{V_i} \sum_f \{A_f^+(U_f^n, U_f^{n+1,s}) S_f\} \right] \cdot \delta U_i^{n,s} + \frac{1}{V_i} \sum_f \{A_f^-(U_f^n, U_f^{n+1,s}) \cdot \delta U_{\text{nbr}}^{n,s} S_f\} \\ & = -\frac{U_i^{n+1,s} - U_i^n}{\Delta t} - \frac{1}{V_i} \sum_f F'_f(U_f^n, U_f^{n+1,s}) S_f. \end{aligned}$$

These equations are solved using the point relaxation method, as before. As the sequence of values  $U^{n+1,s}$  converges to a limiting value (the ‘solution’,  $U^{n+1}$ ), the LHS of the discretized equation above becomes zero and we are left with the desired conservation form

$$\frac{U_i^{n+1} - U_i^n}{\Delta t} - \frac{1}{V_i} \sum_f F'_f(U_f^n, U_f^{n+1}) S_f = 0.$$

Note that if the sub-iteration process truly drives  $\delta U^{n,s}$  close to zero, the implicit dissipation terms (Eq. (22)) also vanish.

The implicit method presented here is not necessarily the most efficient one. Convergence acceleration can be achieved by using various preconditioning techniques (both matrix and low Mach number preconditioning), and by the use of a more

efficient linear solver. Using a Newton–Krylov solver with block Jacobi preconditioning, for example, gives us a speedup of around a factor of three. However, the point relaxation algorithm discussed in this section has the advantage of being simple and easily reproducible without being too inefficient.

## 5. Results

### 5.1. Shock tube problem

A one-dimensional shock tube problem is computed to illustrate that the fluxes are conservative and that the shock capturing mechanisms function adequately. At  $t = 0$ , the conditions to the left and right of the initial discontinuity are specified as  $(\rho_l, p_l, u_l) = (1, 1, 0)$  and  $(\rho_r, p_r, u_r) = (0.125, 0.1, 0)$ . The domain is of unit length and the initial jump is located at the mid-point (this is Sod's shock tube problem). The solution is advanced to  $t = 0.2$ , at which point an expansion, a contact discontinuity and a shock should be clearly seen. Fig. 2(a) shows the result of an Euler calculation on a 100 point grid. The shock capturing is done using a TVD-MUSCL scheme combined with the switched dissipation method mentioned in Section 3. For one-dimensional problems, the Ducros switch (Eq. (12)) is not useful since the vorticity is undefined; an alternate switch based on pressure and density gradients which can detect the shock is used instead. The solution is identical to that obtained using a standard shock capturing scheme and the shock location is correctly predicted. The exact solution to the problem is also plotted, for comparison. Fig. 2(b) is the result of running a Navier–Stokes calculation on a finer mesh, of 500 points, with the shock capturing mechanism switched off everywhere. The Reynolds number used is 2000, based on the initial sound speed to the left of the jump and the length of the domain. The sharp gradients that are present have been cleanly captured, without any ‘ringing’ or spurious oscillations. (see also the recent paper by Jameson [36]). The implicit time integration scheme was used and the time step used in the calculations corresponds to a CFL number of approximately 1.2. To give an idea of the cost of the implicit scheme, we note that the average number of relaxation iterations and the number of sub-iterations required to drive the residual down by three orders of magnitude from its initial value were 5 and 4, respectively.

### 5.2. Hypersonic double-cone flow

The hypersonic flow over double-cone geometries displays many of the complex phenomena such as shock interactions, triple points and recirculation zones that are found in flow past hypersonic vehicles. This case is meant to demonstrate that the low-dissipation numerics are capable of dealing with strong shocks and shock/shock interactions that are typical of these flows.

This hypersonic Mach number flow case corresponds to the simulations of Nompelis [37]; the flow conditions are obtained from the 25°–55° double-cone experiments of Holden and Wadhams [38] and Harvey et al. [39] (“Case 35” in their notation). The freestream conditions are

$$T_\infty = 138.9 \text{ K}, \quad \rho_\infty = 5.515 \times 10^{-4} \text{ kg m}^{-3} \quad \text{and} \quad u_\infty = 2713 \text{ m/s},$$

which gives a freestream Mach number of 11.3 and a unit Reynolds number of  $1.3 \times 10^5 \text{ m}^{-1}$  (Sutherland's law is used to determine the viscosity). The double-cone geometry has two conical sections, each of length 10.16 cm. An attached shock is formed at the leading edge of the first cone and a detached bow shock ahead of the second one; their interaction produces a transmitted shock wave that impinges on the surface of the second cone. The flow separates at the junction of the two

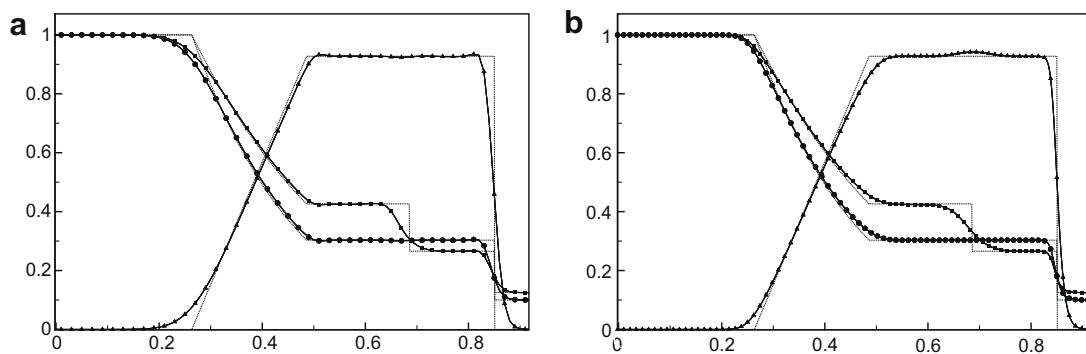


**Fig. 2.** Sod's shock tube problem: (a) Euler calculation on a 100 point grid using a pressure-gradient based switch as shock detector. (b) Navier–Stokes calculation on 500 point grid;  $Re = 2000$ . Dotted lines: exact inviscid solution at  $t = 0.2$ . ■: density, ▲: velocity, ●: pressure.

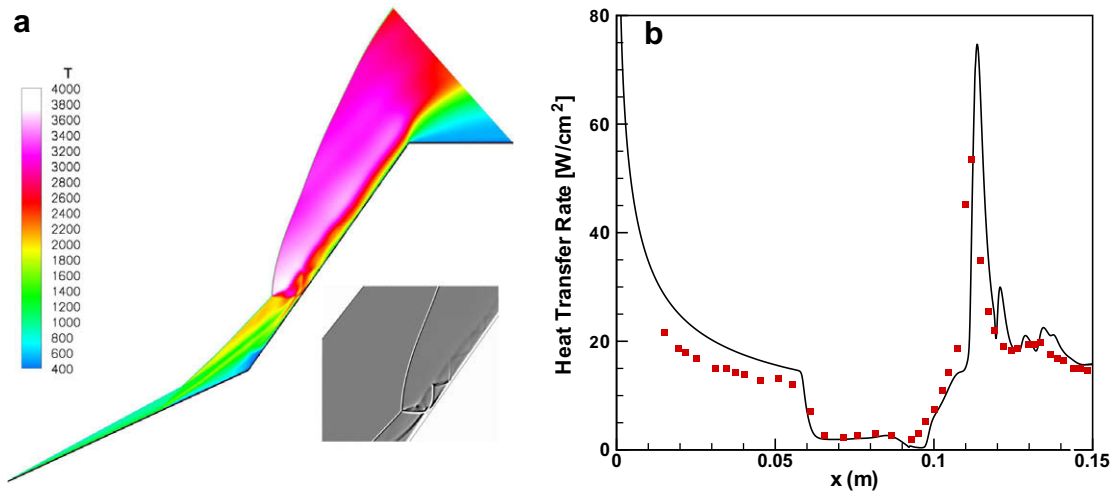


**Fig. 3.** Double-cone in hypersonic flow. (a) Temperature contours ( $1024 \times 512$  grid). Inset shows the numerical shadowgraph of the shock interaction region. (b) Heat transfer rate at the surface. Symbols: experiment, solid line: computation.

cones and the recirculating region in turn alters the shock interactions. The size of the recirculation region is sensitive to the levels of artificial dissipation in the numerical method [40].

The boundary conditions are supersonic inflow, no-slip isothermal-wall ( $T_w = 296$  K) and simple extrapolation at the out-flow boundary. The grid size used in the calculation here was  $1024 \times 512 \times 2$  (1024 points along the surface, 512 points in the direction normal to it and 2 points in the tangential direction). To generate the grid, a 2D grid (of size  $1024 \times 512$ ) is swept by a small angle about the cone axis, to form a slice of the axisymmetric 3D geometry (symmetry boundary conditions are applied at the lateral surfaces). The grid is clustered at the walls. The time step used in this case was relatively large: the CFL number is ramped up to a maximum value of  $10^5$ . Note that the low-dissipation form of the fluxes are used (TVD-MUSCL with the minmod limiter and the Ducros switch). Fig. 3(a) shows temperature contours in a slice of the flow. The inset in the figure shows a numerical shadowgraph (using the Laplacian of the density field) of the shock interaction region. The relatively complex shock interaction is well represented. The heat transfer rate along the surface of the cone is plotted in Fig. 3(b). Note that, in the forebody region, in order to obtain a good match with experimental results when the freestream conditions mentioned above are used, the effect of vibrational relaxation and chemical reactions must be considered. Agreement with the simulations in [37] is excellent.

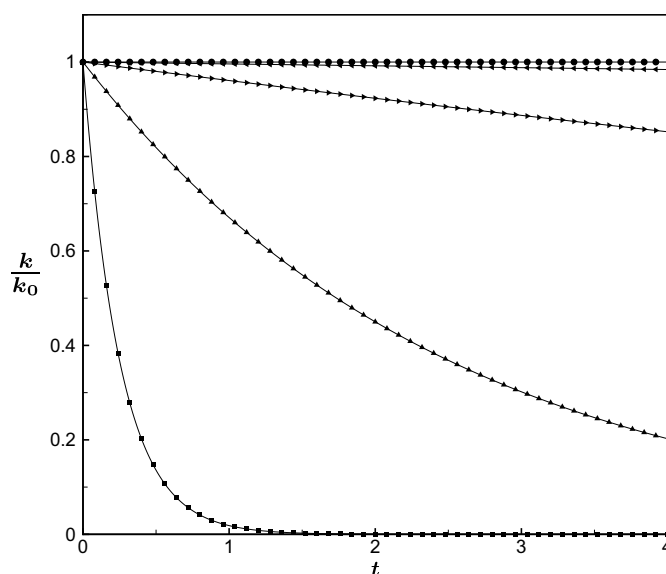


**Fig. 4.** Taylor problem, decay of kinetic energy vs. time at various Reynolds numbers. Solid lines are the analytical curves. Symbols are from computation. Symbols:  $\blacksquare$ :  $Re = 1$ ,  $\blacktriangle$ :  $Re = 10$ ,  $\bullet$ :  $Re = 10^2$ ,  $\blacklozenge$ :  $Re = 10^3$ ,  $\bullet$ :  $Re = \infty$ .

### 5.3. Taylor–Green problem

The Taylor problem describes counter-rotating vortices that decay in time at a rate governed by the viscosity. It is an analytical solution to the incompressible Navier–Stokes equations, and for a 2D domain of size ( $L_x = 2\pi, L_y = 2\pi$ ), the solution is given by

$$u = -\cos(x) \sin(y) e^{-2\nu t}, \quad v = \sin(x) \cos(y) e^{-2\nu t}, \quad p = p_0 - \frac{1}{4}(\cos(x) + \cos(y)) e^{-4\nu t},$$

where  $\nu$  is the kinematic viscosity and the value  $p_0$  essentially determines the initial mean Mach number of the problem. The problem is a simple test of the robustness of a numerical algorithm. Mahesh et al. [26] show that, for incompressible flows, central schemes that do not conserve kinetic energy cause the solution to blow-up at high Reynolds numbers (see also [41]).

Here, the mean Mach number was chosen to be 0.01 and the flow was initialized using the known solution. The grid size used is  $32 \times 32$  and the time step in this case was 0.01, which gave a CFL number (based on the maximum wave speed,  $|u| + c$ ) of around 4. The dissipation terms are turned off ( $\alpha_{\text{diss}} = 0$ ). Fig. 4 shows the evolution of kinetic energy versus time for Reynolds numbers ranging from 1 to  $\infty$  (inviscid). The comparison with the known analytical solution is essentially exact and the method is robust at extremely high Reynolds numbers.

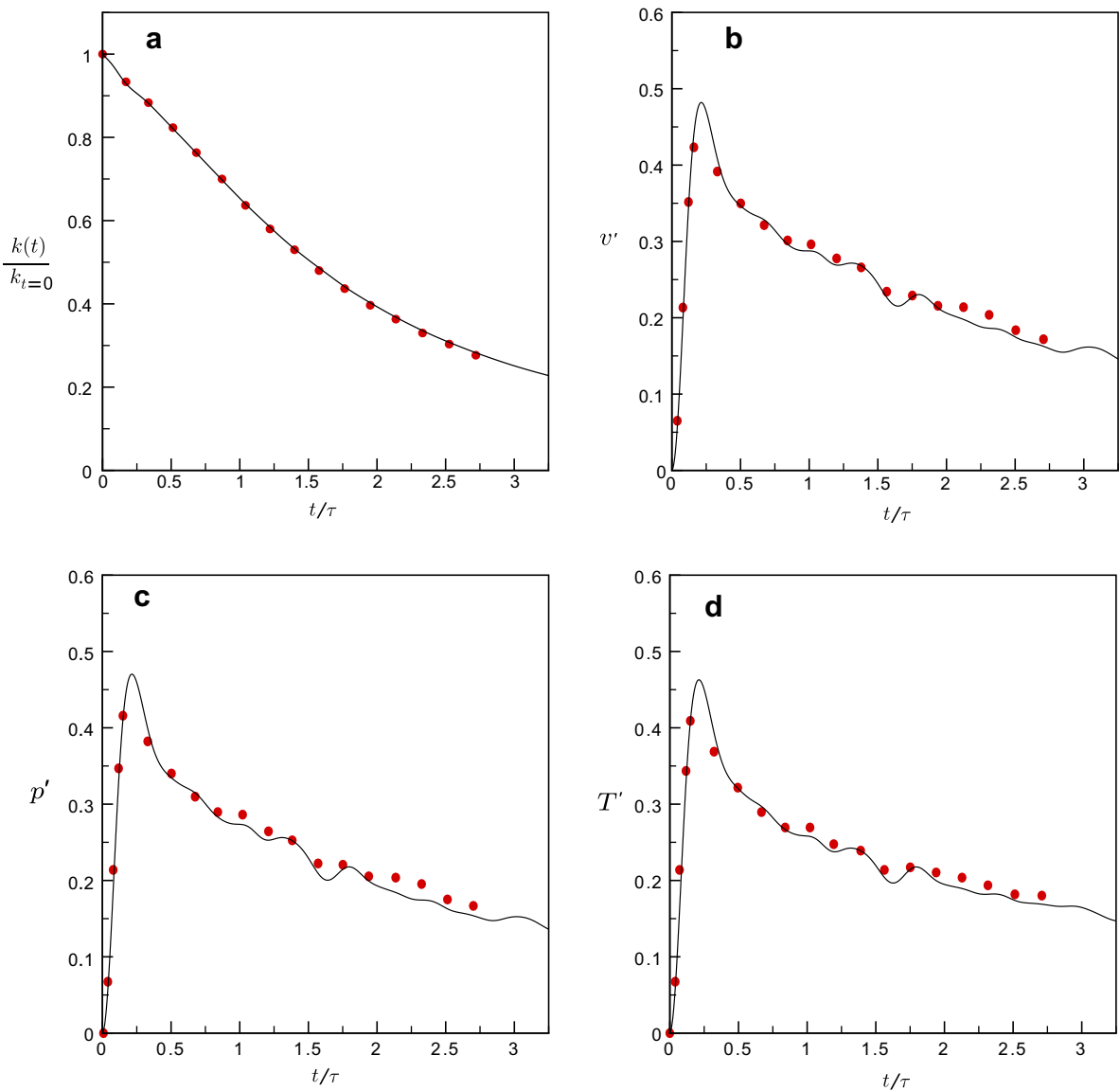


**Fig. 5.** DNS of compressible isotropic turbulence. Time evolution of (a) kinetic energy, (b) RMS specific volume  $v'$ , (c) RMS pressure and (d) RMS temperature. Symbols correspond to a de-aliased spectral computation (from [25]) and solid lines are the result of our computations.

#### 5.4. Isotropic turbulence: DNS at low $Re_\lambda$

A resolved simulation of compressible isotropic turbulence is performed to validate the numerics. The initial Reynolds number based on the Taylor microscale is  $Re_\lambda = 30$ , the initial fluctuating Mach number,  $M_{t0}$ , is 0.3 and the grid has  $64^3$  points. For this low  $Re$ , the grid resolution is considered to be adequate for a DNS. The conditions are the same as those of [42 and 25]. The initial energy spectrum is given by

$$E(k) = \frac{16}{3} \sqrt{\frac{2}{\pi}} M_{t0}^2 \frac{k^4}{k_0^4} e^{-2k^2/k_0^2}, \quad k_0 = 4.$$

The given spectrum is used to generate a divergence-free, random initial velocity field using the method of Rogallo [43]. The thermodynamic variables are initialized with uniform values and the time step used corresponds to a CFL of  $\approx 1$  for this case. Note that the dissipative terms are turned off.

The evolution of the non-dimensional turbulent kinetic energy and RMS values of pressure ( $p'$ ), specific volume ( $v'$ ) and temperature ( $T'$ ), defined as

$$p' = \frac{p_{rms}}{\gamma p_0 M_{t0}^2}, \quad T' = \frac{T_{rms}}{(\gamma - 1) T_0 M_{t0}^2} \quad \text{and} \quad v' = \frac{v_{rms}}{v_0 M_{t0}^2},$$

are shown in Fig. 5. They are compared with data from [25] where results obtained using a de-aliased spectral method are given. The agreement is reasonable.

#### 5.5. Isotropic turbulence: coarse grid simulations

High Reynolds number LES/DES of flows in complex geometries are typically done on relatively coarse meshes. Under-resolved simulations of isotropic turbulence are representative of these conditions and are a good test of the robustness of a numerical method. These types of simulations were performed for incompressible flow in [26] and for compressible flow in [25,41], among others.

##### 5.5.1. Robustness at high Reynolds numbers

The initial conditions are generated in the same manner as with the DNS described in the previous section. The fluctuating Mach number for these cases is  $M_{t0} = 0.07$  and  $k_0 = 6$  – the conditions correspond exactly to those of [25], who make extensive comparisons of their numerical scheme with several other methods. They note that for these simulations, the kinetic energy and thermodynamic quantities decay at a rate determined by the Reynolds number for finite  $Re_\lambda$ , but remain approximately constant (after a short transient) for  $Re_\lambda \rightarrow \infty$ . Using de-aliased spectral simulations of the Euler equations, they determined that as  $Re_\lambda \rightarrow \infty$ , the non-dimensional thermodynamic quantities reach an approximately constant value,  $v' \approx p' \approx T' \approx 0.35$ , and that the non-dimensional kinetic energy stays constant ( $k/k_0 \approx 1$ ). The interesting point is that most of the numerical schemes considered in their paper do not produce results consistent with these observations; typically the kinetic energy is not bounded at high  $Re_\lambda$  and the rms values of the thermodynamic variables diverge.

The time evolution of the kinetic energy and fluctuating temperature is shown in Fig. 6. Note that at high  $Re_\lambda$ , the kinetic energy stays bounded and for the inviscid case ( $Re_\lambda = \infty$ ), stays constant. The fluctuating temperature has the expected behavior when the Reynolds number is varied. For the inviscid case,  $T'$ , as well as the other fluctuating thermodynamic variables reach values of  $\approx 0.31$  which is fairly close to that predicted by spectral simulations. The only discrepancy is that in our simulations, there is a sharp peak during the transient stage, where  $T'$  reaches a larger value than that shown in their paper.

##### 5.5.2. Effect of dissipative fluxes

Note that the dissipation terms are switched off in the previous isotropic turbulence cases considered. In most simulations, switching these terms off is not an option; even if there are regions in a flow where shock capturing is not required, the switches we use to detect them are not perfect. The hope is that using the low-dissipation shock capturing schemes would help in reducing the dissipation levels substantially, without compromising the shock capturing capability.

##### Case A: low Mach number

Here, we consider a decaying isotropic turbulence simulation at  $32^3$  resolution with conditions corresponding to the Comte-Bellot–Corrsin [44] experiment. The paper provides data from experiments on decaying, grid generated isotropic turbulence. The decay is actually spatial, but Taylor's hypothesis can be used to compare these results with temporally decaying turbulence in a periodic box. Spectra at three stations corresponding to non-dimensional times  $tU_0/M = 42, 98$  and 171 are provided ( $U_0$  is the freestream velocity and  $M$  is the spacing in the mesh used to generate the turbulence). The Reynolds number at the initial time is  $Re_\lambda \approx 72$ .

The initial fluctuating Mach number is set to 0.1 and the experimental spectrum at  $tU_0/M = 42$  is used to initialize the flow field using Rogallo's method. The grid resolution is completely inadequate for this value of  $Re_\lambda$  – a turbulence model is required to capture the actual decay. We present results from inviscid simulations, Navier–Stokes simulations (without

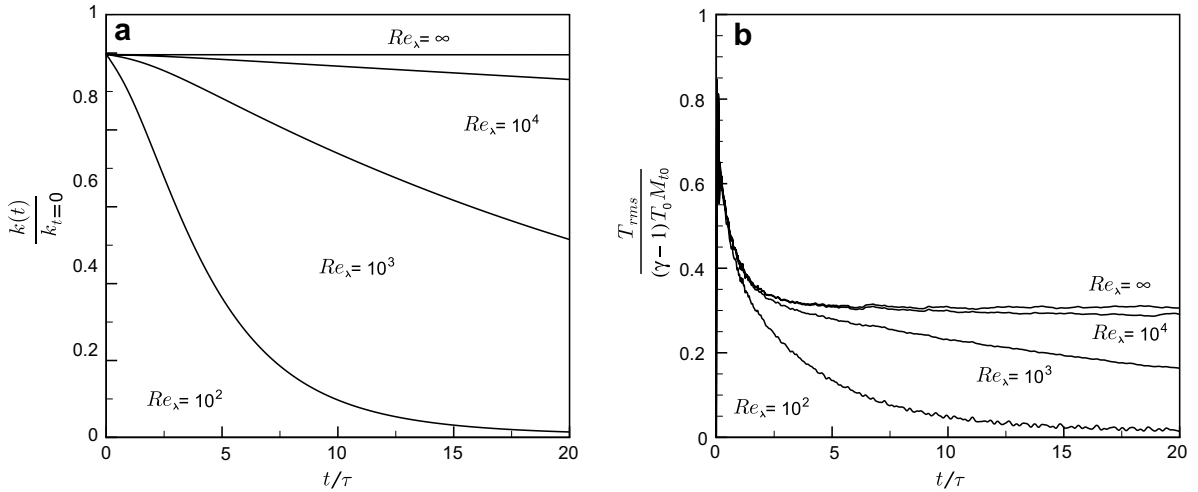


**Fig. 6.** Under-resolved isotropic turbulence ( $M_{i0} = 0.07$ ,  $k_0 = 6$ ). Time evolution of (a) kinetic energy and (b) RMS temperature for a range of  $Re_\lambda$ .

a turbulence model) and LES calculations to gauge the levels of dissipation that are present with and without the low-dissipation switches. The SGS stresses and the turbulent heat flux in the LES calculations are modeled using the dynamic Smagorinsky model,

$$\tau_{ij} - \frac{\delta_{ij}}{3} \tau_{kk} = -2C_s \rho \Delta^2 |S| \left( S_{ij} - \frac{1}{3} S_{kk} \delta_{ij} \right), \quad \tau_{kk} = 2C_i \rho \Delta^2 |S|^2, \quad q_j = -\rho \frac{C_s \Delta^2 |S|}{Pr_T} \frac{\partial T}{\partial x_j},$$

where  $S_{ij} = (\partial u_i / \partial x_j + \partial u_j / \partial x_i) / 2$ ,  $|S| = \sqrt{2 S_{ij} S_{ij}}$ ,  $\Delta = (\Delta x \Delta y \Delta z)^{1/3}$ . The coefficients  $C_s$ ,  $C_i$  and  $Pr_T$  are determined dynamically using the Germano identity (as in Moin et al. [45] with the modification due to Lilly [46]). The test filtering is done over the face neighbors of each cell using a discrete form of the top-hat filter. For the isotropic turbulence cases in this paper, the spatial averaging over homogeneous directions, which is necessary to avoid instability, is performed over the whole domain.

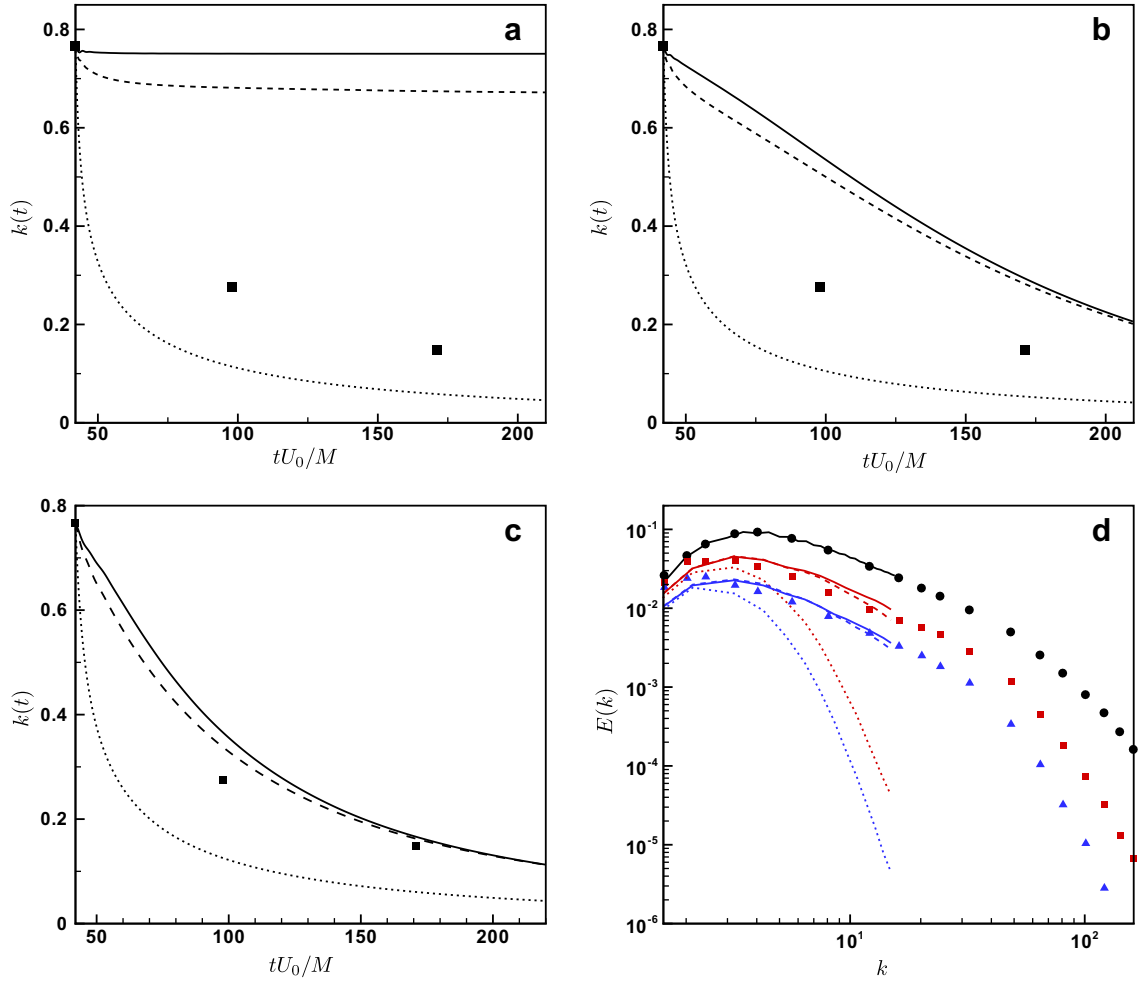
Fig. 7 shows the decay of kinetic energy for three values of the dissipation switch: (i) zero dissipation,  $\alpha_{diss} = 0$  (ii) ‘low-dissipation’ fluxes which use the Ducros switch (Eq. (12)) for  $\alpha_{diss}$ , and (iii) fully dissipative fluxes with  $\alpha_{diss} = 1$ . The left and right states used in the dissipative flux are constructed using the MUSCL scheme with the minmod limiter. The time step used corresponds to a CFL of  $\approx 2$ .

Fig. 7(a–c) shows the decay of kinetic energy with time from the Euler, Navier–Stokes (no model) and LES simulations, respectively. The results highlight the striking levels of numerical dissipation due to undamped shock capturing schemes. Lowering the dissipation levels with the Ducros switch helps a great deal – the no-model viscous simulation results for the zero dissipation case and the low-dissipation case are reasonably close to each other, although a difference is still apparent. When the turbulence model is switched on, the amount of numerical viscosity introduced by the switched dissipation terms is negligible compared to the eddy viscosity. This is further confirmed by the energy spectra plots in Fig. 7(d).

#### Case B: higher Mach number

Since the initial Mach number used in the simulation above is low, shock waves do not form in the domain and the shock detection switch takes on low values everywhere. Here, we consider a simulation at an initial turbulent Mach number of 0.5. For this case, shock waves form almost immediately after startup. Since no experimental data exists for these conditions, we first perform a DNS on a  $128^3$  point grid (the initial Reynolds number is  $Re_\lambda = 72$  and  $k_0 = 4$ ). The results of the DNS match well with similar computations done by Samtaney et al. [10]. Fig. 8(a) shows iso-lines of the fluctuating density (dashed lines correspond to negative values) superimposed on contours of the dilatation (large negative values are plotted) at non-dimensional time  $t/\tau \approx 0.75$ . This time instant is the point when the kurtosis of the velocity divergence reaches a peak (the kurtosis is good indicator since a large deviation of the dilatation flatness from 3 will indicate the presence of shocklets). The figure indicates the presence of shocklets.

The DNS results are now compared to LES on a  $32^3$  grid (the dynamic Smagorinsky model is used). Fig. 8(b) compares the decay of kinetic energy with time for three values of the dissipation switch, as in the previous case: (i) zero dissipation,  $\alpha_{diss} = 0$ , (ii) ‘low-dissipation’ fluxes which use the Ducros switch (Eq. (12)) for  $\alpha_{diss}$ , and (iii) fully dissipative fluxes with  $\alpha_{diss} = 1$ . The results match reasonably well with the decay rate predicted by the (filtered) DNS. Fig. 8(b) and (c) shows the velocity and dilatation spectra at  $t/\tau \approx 0.75$ , respectively. Note that the dilatation spectrum for the zero-dissipation case diverges from the DNS result, whereas the ‘low-dissipation’ switch performs rather well. This strongly suggests that the shock capturing is well localized and the shock detector works as intended.



**Fig. 7.** (a–c): Decay of kinetic energy. (a) Euler simulations ( $Re = \infty$ ). (b) Navier–Stokes simulations with no turbulence model. (c) LES with dynamic Smagorinsky model. (d) Energy spectra at  $tU_0/M = 42, 98, 171$  (LES with dynamic Smagorinsky model). Solid lines:  $\alpha_{diss} = 0$ , dashed lines:  $\alpha_{diss} \equiv$  Ducros switch, dotted lines:  $\alpha_{diss} = 1$ , symbols: values from Comte-Bellot–Corrsin experiment. In (d), symbols ( $\bullet$ ,  $\blacksquare$ ,  $\blacktriangle$ ) correspond to  $(tU_0/M = 42, 98, 171)$ , respectively.

### 5.6. Compressible channel flow

As a final test case, we consider a supersonic isothermal-wall compressible channel flow. Results are compared with the DNS study of this problem by Coleman et al. [47]. The flow is driven using a fixed uniform body force which appears as a source term in the momentum and energy equations. Since the body force is fixed, the bulk velocity ( $u_b$ ) and wall shear stress vary with time, oscillating about a roughly constant value after the flow reaches a statistically stationary state. The viscosity is assumed to follow a power law with an exponent of 0.7,  $\mu \propto (T/T_w)^{0.7}$ , where  $T_w$  is the constant wall temperature. The Prandtl number is set to 0.7. The Reynolds number based on the bulk density, bulk velocity and the viscosity at the wall is 3000 and the Mach number based on the bulk velocity and speed of sound (based on the wall temperature) is 1.5. The flow is initialized using random noise (of maximum amplitude  $0.2u_b$ ) superimposed on the laminar velocity profile. The dissipative terms are turned off and the time step corresponds to a CFL of  $\approx 2$ .

The size of the domain is  $[L_x = 4\pi, L_y = 4\pi/3, L_z = 2]$ , where  $x$  and  $z$  are the streamwise and wall-normal directions, respectively. The grid, which has  $100 \times 100 \times 100$  points, is uniformly spaced in the  $x, y$  directions and stretched in the wall-normal direction using a hyperbolic tangent function,

$$z_k = \frac{\tanh[c(2(k-1)/(n_z-1)-1)]}{\tanh(c)}.$$

The constant  $c$  was chosen to be 1.7 for this example. Expressing the grid spacings in wall units gives  $\Delta x^+ \approx 24$ ,  $\Delta y^+ \approx 8$  and the first point off the wall is at a height  $\Delta z^+ \approx 0.9$ . The streamwise and spanwise grid spacings are comparable to those used in the DNS of [47] and the wall-normal spacing is coarser (there are 8 points within  $0 < y^+ < 8$ ; by comparison, in [47], the first point off the wall is at  $y^+ = 0.1$  and there are 10 points below  $y^+ = 8$ ).



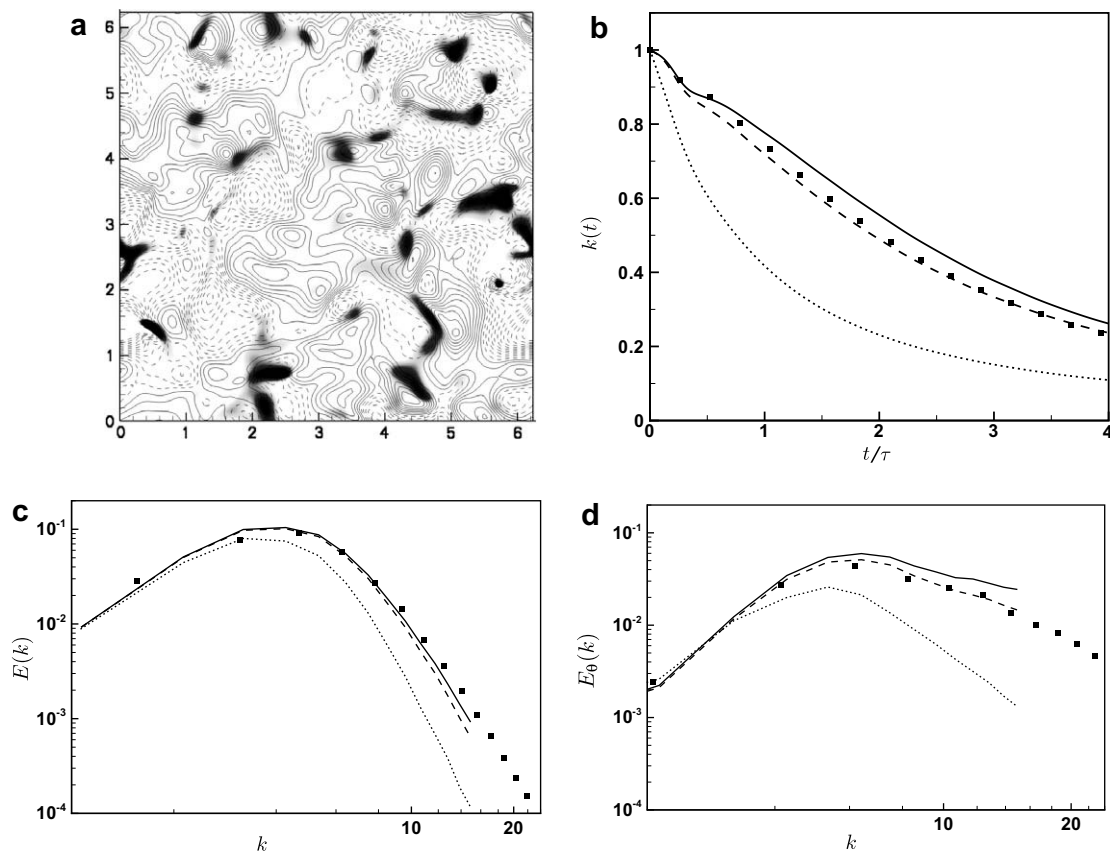


**Fig. 8.** (a) DNS: Isolines of  $\rho - \bar{\rho}$  (dashed lines correspond to negative values) superimposed on contours of dilatation (values of  $\theta < -\theta'$  are shown). (b) Decay of kinetic energy with time (symbols are filtered DNS data). (c) Velocity spectra. (d) Dilatation spectra. For (b–d), Solid lines:  $\alpha_{\text{diss}} = 0$ , dashed lines:  $\alpha_{\text{diss}} = 1$ , symbols: DNS data.

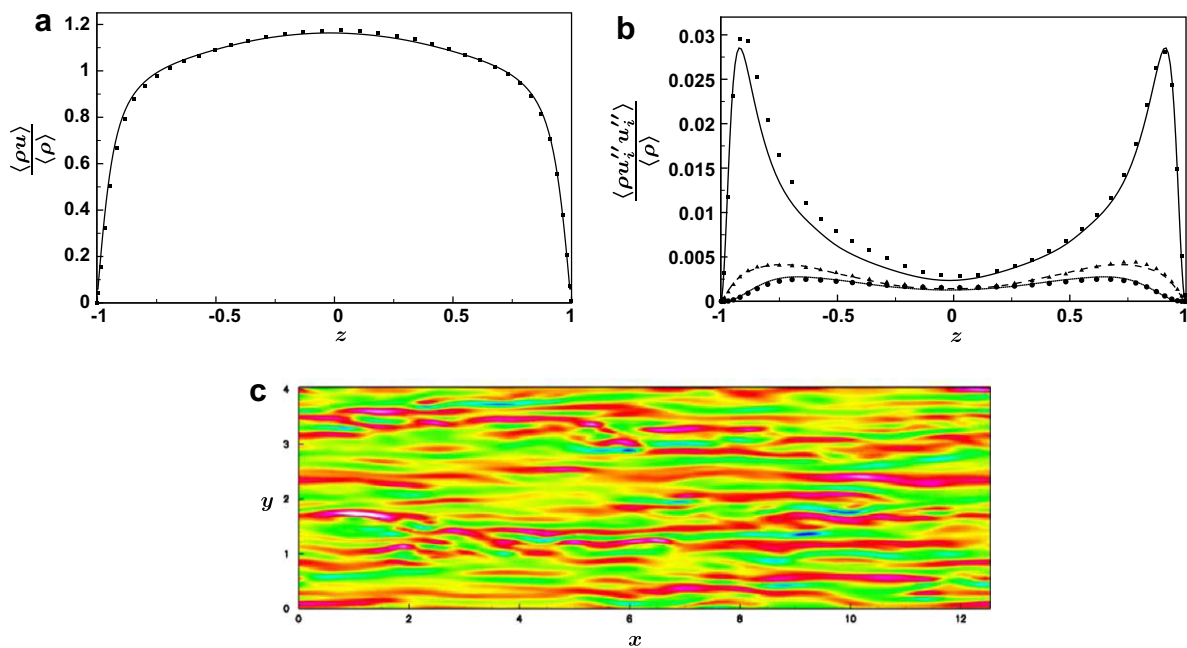


**Fig. 9.** Compressible channel flow. (a) Mean velocity profile. (b) Turbulent normal stresses. (c) Wall normal vorticity contours in a plane at distance 0.04 units from the wall.

Fig. 9(a) shows the time and Favre averaged velocity profile compared with the DNS (note that the velocity is normalized by the mean bulk velocity in the plots). The mean centerline velocity is 1.163 which compares well with the value 1.175 predicted by the DNS. Fig. 9(b) compares the predicted turbulent normal stresses (double primes denote fluctuations about a Favre averaged quantity:  $f'' = f - \langle \rho f \rangle / \langle \rho \rangle$ ). The agreement is quite reasonable. Finally, Fig. 9(c) shows contours of the wall normal vorticity on an  $x$ - $y$  plane at a distance 0.04 units from one of the walls. This is meant to serve as a qualitative comparison with a similar plot in [47] which shows  $\omega_z$  contours at the same plane; the figures are strikingly similar.

## 6. Summary

We have presented an implicit second-order scheme for turbulent compressible flow suitable for DNS/LES applications. For problems without shocks, the method is robust and does not need artificial dissipation, upwinding or filtering. For flows with shocks, using a shock detecting switch gives results that have low levels of dissipation without compromising the shock capturing capability. Numerical test problems included decaying isotropic turbulence, channel flow simulations and the hypersonic flow over a double-cone geometry. The method is easily adaptable to unstructured grid solvers and shows potential for use in LES/DNS of realistic problems.

## Acknowledgments

The authors would like to thank Professor Gary N. Coleman for the channel flow DNS data and Dr. Ioannis Nompelis for help with the double-cone simulations. The research is supported by Air Force Office of Scientific Research (AFOSR) under Grant No. FA9550-0401-0341 and the NASA Fundamental Aeronautics Program. The views and conclusions contained herein are those of the authors and should not be interpreted as necessarily representing the official policies or endorsements, either expressed or implied, of the AFOSR or the US Government.

## References

- [1] H. Yee, N. Sandham, M. Djomehri, Low-dissipative high-order shock-capturing methods using characteristic-based filters, *Journal of Computational Physics* 150 (1) (1999) 199–238.
- [2] F. Ducros, V. Ferrand, F. Nicoud, C. Weber, D. Darracq, C. Gacherieu, T. Poinsot, Large-eddy simulation of shock/turbulence interaction, *Journal of Computational Physics* 152 (2) (1999) 517–549.
- [3] A. Jameson, W. Schmidt, E. Turkel, Numerical solution of the Euler equations by the finite volume method using Runge–Kutta time-stepping schemes, *AIAA Paper* 1981-1259, 1981.
- [4] M. Gerritsen, P. Olsson, Designing an efficient solution strategy for fluid flows. II. Stable high-order central finite difference schemes on composite adaptive grids with sharp shock resolution, *Journal of Computational Physics* 147 (2) (1998) 293–317.
- [5] B. Sjögreen, H. Yee, Multiresolution wavelet based adaptive numerical dissipation control for high order methods, *Journal of Scientific Computing* 20 (2) (2004) 211–255.
- [6] N. Phillips, An example of nonlinear computational instability, in: Bert Bolin (Ed.), *The Atmosphere and the Sea in motion*, 1959, pp. 501–504.
- [7] S. Orszag, On the elimination of aliasing in finite-difference schemes by filtering high-wavenumber components, *Journal of Atmospheric Sciences* 28 (6) (1971) 1074.
- [8] G. Blaisdell, E. Spyropoulos, J. Qin, The effect of the formulation of nonlinear terms on aliasing errors in spectral methods, *Applied Numerical Mathematics* 21 (3) (1996) 207–219.
- [9] F. Ducros, F. Laporte, T. Souères, V. Guinot, P. Moinat, B. Caruelle, High-order fluxes for conservative skew-symmetric like schemes in structured meshes: Application to compressible flows, *Journal of Computational Physics* 161 (1) (2000) 114–139.
- [10] R. Samtaney, D. Pullin, Kosović, Direct numerical simulation of decaying compressible turbulence and shocklet statistics, *Physics of Fluids* 13 (5) (2001) 1415–1430.
- [11] C. Pantano, R. Deiterding, D. Hill, D. Pullin, A low-numerical dissipation patch based adaptive mesh refinement method for large-eddy simulation of compressible flows, *Journal of Computational Physics* 221 (1) (2007) 63–87.
- [12] E. Lenormand, P. Sagaut, L. Ta Phuoc, P. Comte, Subgrid-scale models for large-eddy simulations of compressible wall bounded flows, *AIAA Journal* 38 (8) (2000) 1340–1350.
- [13] R. von Kaenel, L. Kleiser, N. Adams, J. Vos, Large-eddy simulation of shock-turbulence interaction, *AIAA Journal* 42 (12) (2004) 2516–2528.
- [14] C. Kennedy, A. Gruber, Reduced aliasing formulations of the convective terms within the Navier–Stokes equations for a compressible fluid, *Journal of Computational Physics* 227 (3) (2008) 1676–1700.
- [15] P. Moin, K. Mahesh, Direct numerical simulation: a tool in turbulence research, *Annual Review of Fluid Mechanics* 30 (1998) 539–578.
- [16] S. Godunov, An interesting class of quasilinear systems, *Doklady Akademii Nauk* 139 (1961) 521–523.
- [17] K. Friedrichs, P. Lax, Systems of conservation equations with a convex extension, *Proceedings of the National Academy of Sciences, USA* 68 (8) (1971) 1686–1688.
- [18] A. Harten, On the symmetric form of systems of conservation laws with entropy, *Journal of Computational Physics* 49 (1) (1983) 151–164.
- [19] E. Tadmor, Skew-self adjoint forms for systems of conservation laws, *Journal of Mathematical Analysis and Applications* 103 (1984) 428–442.
- [20] M. Mock, Systems of conservation laws of mixed type, *Journal of Differential Equations* 37 (1980) 70–88.
- [21] P. Olsson, Energy and maximum norm estimates for nonlinear conservation laws, *Tech. Rep. RIACS 94-01*, RIACS, 1994.
- [22] M. Gerritsen, P. Olsson, Designing an efficient solution strategy for fluid flows. I. A stable high-order finite difference scheme and sharp shock resolution for the Euler equations, *Journal of Computational Physics* 129 (2) (1996) 245–262.
- [23] E. Tadmor, The numerical viscosity of entropy stable schemes for systems of conservation laws. I, *Mathematics of Computation* 49 (1987) 91–103.
- [24] P. Roe, Affordable entropy-consistent Euler flux functions, in: *Eleventh International Conference on Hyperbolic Problems: Theory, Numerics, Applications*, Lyons, France, July 2006. <<http://math.univ-lyon1.fr/hyp2006/outputs/Roe-slides.pdf>>.
- [25] A. Honein, P. Moin, Higher entropy conservation and numerical stability of compressible turbulence simulations, *Journal of Computational Physics* 201 (2) (2004) 531–545.
- [26] K. Mahesh, G. Constantinescu, P. Moin, A numerical method for large-eddy simulation in complex geometries, *Journal of Computational Physics* 197 (1) (2004) 215–240.
- [27] P. Roe, Approximate Riemann solvers, parameter vectors, and difference schemes, *Journal of Computational Physics* 43 (2) (1981) 357–372.

- [28] C. Wall, C. Pierce, P. Moin, A semi-implicit method for resolution of acoustic waves in low Mach number flows, *Journal of Computational Physics* 181 (2) (2002) 545–563.
- [29] C. Hirsch, *Numerical Computation of Internal and External Flows*, vol. 2, John Wiley and Sons, 1990.
- [30] S. Jaisankar, S. Raghurama Rao, Diffusion regulation for Euler solvers, *Journal of Computational Physics* 221 (2) (2007) 577–599.
- [31] R. MacCormack, G. Candler, The solution of the Navier–Stokes equations using Gauss–Seidel line relaxation, *Computers and Fluids* 17 (1) (1989) 135–150.
- [32] H. Yee, A class of high-resolution explicit and implicit shock-capturing methods, Tech. Rep. TM-101088, NASA, February 1989.
- [33] C.D. Pierce, Progress-variable approach for large eddy simulation of turbulent combustion, Ph.D. thesis, Stanford University, USA, 2001.
- [34] M. Wright, G. Candler, M. Prampolini, Data parallel lower-upper relaxation method for the Navier–Stokes equations, *AIAA Journal* 34 (7) (1996) 1371–1377.
- [35] J. Kim, O. Kwon, An efficient and robust implicit operator for upwind point Gauss–Seidel method, *Journal of Computational Physics* 224 (2) (2007) 1124–1144.
- [36] A. Jameson, Formulation of kinetic energy preserving conservative schemes for gas dynamics and direct numerical simulations of one-dimensional viscous compressible flow in a shock tube using entropy and kinetic energy preserving schemes, *Journal of Scientific Computing* 34 (2) (2008) 188–208.
- [37] I. Nompelis, Computational study of hypersonic double-cone experiments for code validation, Ph.D. thesis, University of Minnesota, USA, 2004.
- [38] M. Holden, T. Wadhams, Code validation study of laminar shock/boundary layer and shock/shock interactions in hypersonic flow. Part A: experimental measurements, AIAA Paper 2001-1031A, 2001.
- [39] J. Harvey, M. Holden, T. Wadhams, Code validation study of laminar shock/boundary layer and shock/shock interactions in hypersonic flow. Part B: comparison with Navier–Stokes and DSMC solutions, AIAA Paper 2001-1031B, 2001.
- [40] M.-C. Druguet, G. Candler, I. Nompelis, Effect of numerics on Navier–Stokes computations of hypersonic double-cone flows, *AIAA Journal* 43 (3) (2005).
- [41] Y. Hou, K. Mahesh, A robust, colocated, implicit algorithm for direct numerical simulation of compressible turbulent flows, *Journal of Computational Physics* 205 (1) (2005) 205–221.
- [42] S. Lee, S. Lele, P. Moin, Simulation of spatially evolving turbulence and the applicability of Taylor's hypothesis in compressible flow, *Physics of Fluids A* 4 (7) (1992) 1521–1530.
- [43] R. Rogallo, Numerical experiments in homogeneous turbulence, Tech. Rep. TM-81315, NASA, 1981.
- [44] G. Comte-Bellot, S. Corrsin, Simple Eulerian time correlation of full and narrow-band velocity signals in grid-generated 'isotropic' turbulence, *Journal of Fluid Mechanics* 48 (1971) 273–337.
- [45] P. Moin, K. Squires, W. Cabot, S. Lee, A dynamic subgrid-scale model for compressible turbulence and scalar transport, *Physics of Fluids A* 3 (11) (1991) 2746–2757.
- [46] D. Lilly, A proposed modification of the germano subgrid-scale closure method, *Physics of Fluids A* 4 (3) (1992) 633–635.
- [47] G. Coleman, J. Kim, R. Moser, A numerical study of turbulent supersonic isothermal-wall channel flow, *Journal of Fluid Mechanics* 305 (1995) 159–183.